Calibration system for satellite and rocket-borne ion mass spectrometers in the energy range from 5 eV/charge to 100 keV/charge

A. G. Ghielmetti, H. Balsiger, R. Bänninger, P. Eberhardt, J. Geiss, and D. T. Young

Physikalisches Institut, University of Bern, CH-3012 Bern, Switzerland

(Received 15 October 1982; accepted for publication 28 December 1982)

A new system has been developed for calibration of space plasma analyzers, in particular ion mass spectrometers. The system provides a large-area (~ 250 cm^2), highly parallel ($\pm 0.5°$), and spatially uniform ($\pm 5\%$) beam of ions over the energy per charge range from 5 eV/charge to 100 keV/charge. Other special features include variable energy spread from $\Delta E \sim 1$ eV/charge to ~ 3 keV/charge and multiple charge state ions such as He^{2+} or Xe^{9+}. Among several key ion optical elements are a high-efficiency electron bombardment ion source capable of delivering $\sim 10^{-8}$ A, a 90° crossed electric and magnetic field mass spectrometer designed to produce either a mixed or a mass-selected beam, and a unique beam expansion system which produces the uniform large-area beam. The system also includes automatic beam monitoring and control via a feedback loop, as well as provisions for semiautomatic control of angle and energy analysis. Use of the calibration system during its development phases has made possible the rapid calibration of five complex satellite ion mass spectrometers already flown. Data from one of these calibrations are discussed here.

PACS numbers: 07.75. + h

INTRODUCTION

An increasing number of new and sophisticated particle analyzers have been developed and applied in the field of space plasma research in recent years.[1] These experiments typically transmit data in the form of detector counting rates, plus fiducial information such as particle energy and detector look direction. To interpret these data in terms of physical parameters (e.g., ion density or temperature) the relationship between count rate and particle distribution function must be known. This relationship, termed the energy-geometric factor, can in principle be derived through ray-tracing calculations. This approach is, however, based on idealized designs and assumptions, and yields results of limited accuracy. It has been applied primarily to the more simple geometries of electrostatic analyzers.[2–6]

The techniques for obtaining energy-geometric factors experimentally involve measuring the instrument response to a particle beam with well-defined properties.[7–9] In the case of conventional electrostatic analyzers this requires measuring in a three-dimensional parameter space consisting of two orthogonal angles and particle energy. In mass spectrometry an additional parameter (mass/charge) is introduced which is qualitatively different from the others. For example, the abundances of minor ion species in space plasmas may be as much as several orders of magnitude lower than those of

TABLE I. Capabilities of calibration facility.

Parameter		Operating values		
Energy range (E/Z)		$\sim$5–100 000	eV/e	
Energy spread ΔE	min	~ 1	eV/e	monoenergetic
	max	$\sim 10^{-3} \times (E/Z)$	eV/e	monoenergetic
	max	3000	eV/e	controlled
Beam cross section		$\sim 28 \times 18$	cm	FWHM
Beam uniformity		± 5	%	over 250 cm^2
Angular collimation		$\lesssim 0.5$	°	full width
Intensity I		$> 10^7$	#/cm^2	broad beam
		$> 10^8$	#/cm^2	narrow beam
Stability ($\Delta I/I$)		± 0.5	%	in 10 h
Mass range (M/Z)		1–150	amu/e	
Charge range Z		1–9	e	
Mass resolution ($M/\Delta M$)		50–100		
Beam purity.		$\sim 10^{-5}$		
Vacuum base pressure		$< 10^{-8}$	Torr	
Experiment parameters:				
Size		$\lesssim 30 \times 40 \times 45$	cm	
Weight		$\lesssim 12$	kg	
View angle	α	$-90°$ to $+90°$		
	β	$-35°$ to $+75°$		

 0034-6748/83/040425-12$01.30

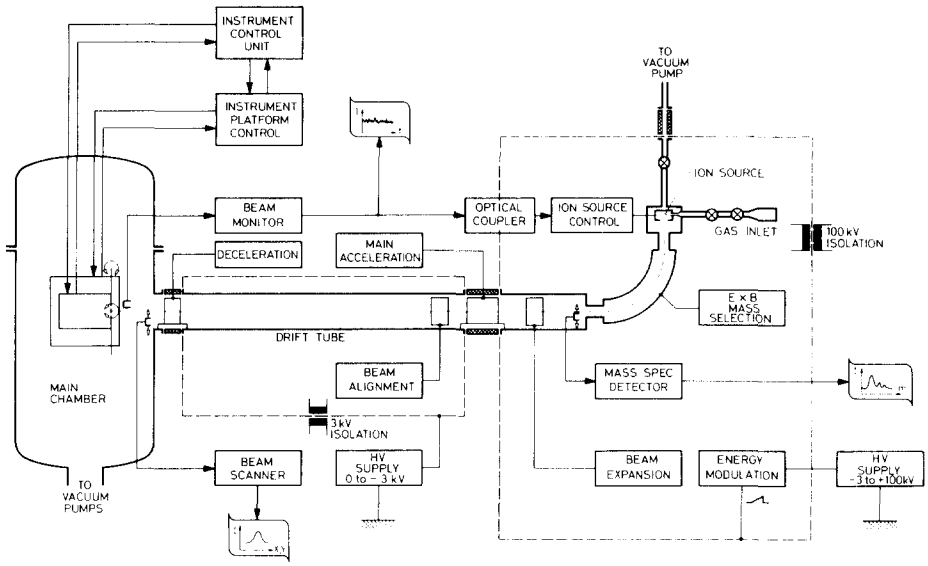

FIG. 1. Schematic diagram of the calibration system.

major species. Unless corrective measures are taken, secondary ions produced by the interaction of major species with internal spectrometer surfaces and stray fields may significantly contaminate the signals of minor ion species. Moreover, secondary ions give rise to spurious ion peaks ("ghosts") in regions of mass-energy space well away from those occupied by the primary ions. To avoid this, it is essential in mass spectrometer calibration to determine any interference at the location of a minor ion to a precision better than the expected abundance ratio. For example, the ratio of $^3He^{2+}$ to H^+ in the solar wind is $\sim 3\times 10^{-5}$.[10] In practice this means a painstaking search of the four-dimensional parameter space in regions away from that occupied by the calibration beam itself. The requirements on mass spectrometer calibration are thus much more complex and stringent than for electrostatic analyzers.

The instrumentation described in this paper was developed for testing and calibrating satellite-borne ion mass spectrometers. Its capabilities are determined largely by the requirements of the latter (Table I). Space plasma instruments typically have sensitive areas $\lesssim 10$ cm^2 with acceptance angles varying from a few degrees to a few tens of degrees. Given the usual detector dynamic range of ~ 0.1–10^6 count/s, we arrive at the beam requirements in Table I. The rationale for this range of parameters is also based on the characteristics of space plasmas, particularly the composition, density, temperature, and resultant fluxes. These are summarized in simplified form in Table II. The very low densities of 10^{-3} cm^{-3} apply to minor constituents (e. g., He^{++}, O^{++}, O^{6+}).

The calibration facility at the University of Bern has thus far been used to design and calibrate ion mass spectrometers flown on five spacecraft (GEOS-1 and -2[11]; ISEE-1[12] and -3[13]; and Dynamics Explorer[14]) and will be employed for several future instruments now under construction, for example, for the International Solar Polar Mission (ISPM), for the Active Magnetospheric Particle Tracer Experiment (AMPTE), and for the GIOTTO cometary mission.[15,16]

I. INSTRUMENTATION

A. Overview

Figure 1 shows a block diagram of the calibration system. To describe the system briefly, ions are produced by an electron bombardment ion source and preaccelerated to an energy of 3 keV/charge. After passing through a mass/charge analyzer which filters out undesired ion species, the beam cross section is expanded by a factor of $\sim 10^3$. The ions are then accelerated or decelerated to their final energy (5–10^5 eV/charge) before entering a drift tube that results in reduction of their angular divergence. The beam is then deflected by high-frequency rastering to uniformly illuminate the target (i.e., the instrument sensor opening) which can be rotated about two perpendicular axes with respect to the beam. Beam current is monitored and automatically kept stabilized during the measurement period by means of a feedback circuit. Several diagnostic probes placed along the beam determine its essential characteristics such as ionic species, intensity profile, and absolute current. The clean UHV chamber operates at pressures $\lesssim 10^{-8}$ Torr and the entire UHV system is placed in a laminar flow clean room that provides the proper environmental conditions for instrument assembly and testing.

TABLE II. Characteristics of space plasmas.

Region	Ions	Density (cm^{-3})	Energy range (eV)
Plasmasphere	H^+, He^{2+}, He^+, O^{2+}, O^+	10^{-2}–10^3	0.2–2
Outer magnetosphere	H^+, He^{2+}, He^+, O^{2+}, O^+	10^{-3}–10	10^2–10^5
Solar wind	H^+, $^4He^{2+}$, O^{6+}, $^3He^{2+}$	10^{-4}–10	0.5–2 keV/amu
Tracer experiments	Li^+, Ba^+ Eu^+ Li^+, Ba^+, Eu^+	$\lesssim 10^{-3}$	10^1–10^5

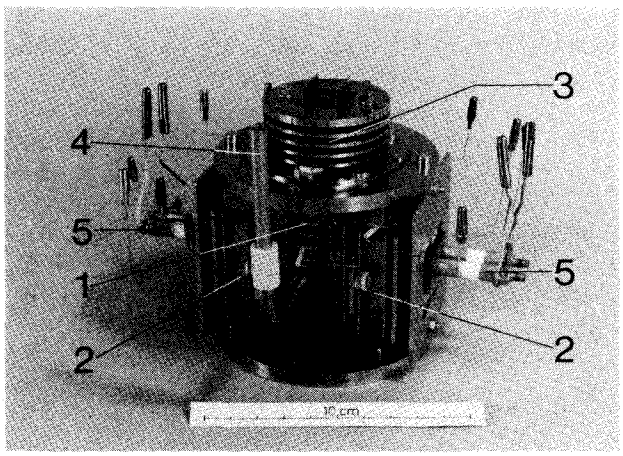

FIG. 2. Photograph of the ion source. (1) Ion gun, (2) electron guns, (3) beam alignment, (4) gas inlet, and (5) cathode mount.

B. Ion source and gas inlet

Design of the ion source (Fig. 2) was optimized primarily to provide multiply charged ions at high efficiency. It is basically an electron bombardment source of the Nier type[17] consisting of an ion gun and two electron guns mounted perpendicular to the ion beam axis. The ion gun ionization chamber (Figs. 3 and 6) is a completely enclosed box with entry and exit apertures for the electron and ion beam, and for the sample gas. A high-transmission grid (92%) placed over the ion extraction slit shields the chamber from strong electric fields in the lens region. The electron beam enters the chamber through a 0.1×0.8-cm rectangular slit traveling perpendicular to the plane of Fig. 3. To efficiently collect and withdraw the ions formed within this region, a cylindrically shaped repeller electrode is used to set up an extraction electric field. This field combines with the field penetrating through the grid to focus the ions in the extraction slit region. The ion beam is then focused on the exit slit of the ion source (0.06×0.6 cm) by means of a single electrostatic lens

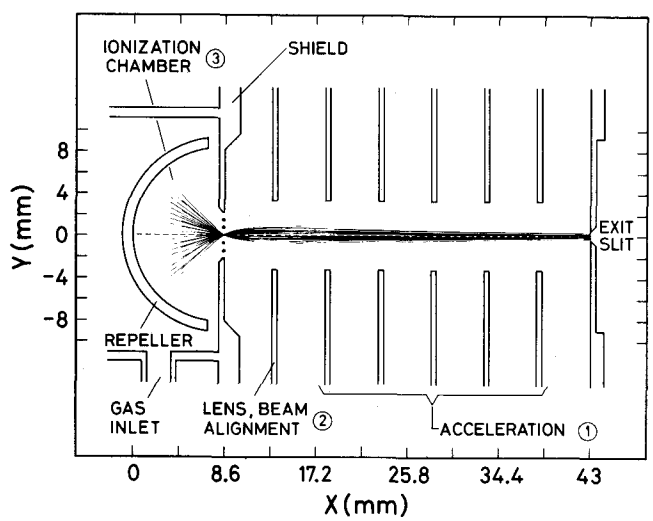

FIG. 3. Cross-sectional view of the ion gun. The electrode geometry was developed with the aid of a numerical potential field and ray tracing computer code. Ion trajectories for zero initial energy were calculated for the following empirical plate voltages: 3 kV on the shield, + 1 V on the repeller, and − 50 V on the lens with respect to the shield.

TABLE III. Ion production efficiencies for various sample gases measured at an e^- emission current of 500 μA and leak gas pressure of 1×10^{-6} Torr. No gauge correction is applied. Units given are ion current in A per Torr per electron emission current in A.

H_2	^{4}He	CH_4	^{20}Ne	C_2H_2	N_2	CO	^{40}Ar	CO_2	^{84}Kr	^{132}Xe
H_2^+ 1.2	He^+ 1.5	CH_4^+ 5.6×10^{-1}	Ne^+ 1.2	$C_2H_2^+$ 1.1	N_2^+ 1.2	CO^+ 1.1	Ar^+ 1.1	CO_2^+ 8.6×10^{-1}	Kr^+ 5.2×10^{-1}	Xe^+ 2.4×10^{-1}
H_3^+ 2.7×10^{-2}	He^{2+} 1.1×10^{-2}	CH_3^+ 2.5×10^{-1}	Ne^{2+} 1.4×10^{-1}	C_2H^+ 2.1×10^{-1}	N^+ 8.4×10^{-2}	O^+ 9.0×10^{-4}	Ar^{2+} 2.5	CO^+ 8.6×10^{-2}	Kr^{2+} 1.4×10^{-1}	Xe^{2+} 6.2×10^{-2}
H^+ 9.8×10^{-3}		CH_2^+ 3.8×10^{-2}	Ne^{3+} 7.8×10^{-3}	C_2^+ 4.7×10^{-2}		CO^{2+} 8.8×10^{-3}	Ar^{3+} 1.3×10^{-2}	CO_2^+ 2.1×10^{-2}	Kr^{3+} 2.3×10^{-2}	Xe^{3+} 4.3×10^{-2}
		CH^+ 1.3×10^{-2}	Ne^{4+} 1.8×10^{-4}	CH^+ 5.5×10^{-2}		C^+ 4.5×10^{-3}	Ar^{4+} 2.8×10^{-3}	O^+ 4.0×10^{-2}	Kr^{4+} 6.8×10^{-3}	Xe^{4+} 6.8×10^{-3}
		C^+ 5.0×10^{-3}	Ne^{5+} 4.9×10^{-6}	C^+ 6.2×10^{-3}			Ar^{5+} 4.0×10^{-4}	CO^{2+} 5.9×10^{-4}	Kr^{5+} 3.1×10^{-3}	Xe^{5+} 2.9×10^{-3}
		H^+ 1.3×10^{-2}		C^{2+} 3.9×10^{-6}			Ar^{6+} 3.6×10^{-5}	C^+ 9.5×10^{-2}	Kr^{6+} 8.8×10^{-4}	Xe^{6+} 7.0×10^{-4}
				H^+ 3.5×10^{-3}			Ar^{7+} 1.5×10^{-6}		Kr^{7+} 1.1×10^{-4}	Xe^{7+} 1.5×10^{-4}
									Kr^{8+} 4.8×10^{-6}	Xe^{8+} 3.1×10^{-5}
										Xe^{9+} 1.2×10^{-6}

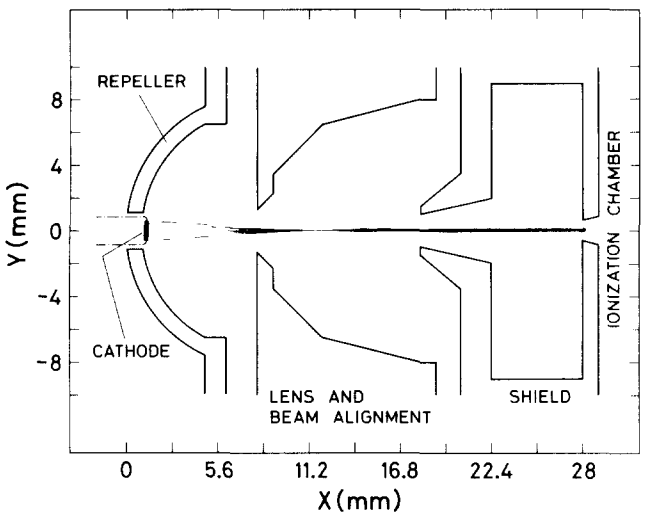

FIG. 4. Schematic cross section through the electron gun with exemplary electron trajectories for the space-charge-free case.

[item (2) in Fig. 3]. A quasihomogeneous acceleration field (1) generated by a set of five parallel plates provides up to 95% of the energy that the ion receives in the source. This arrangement minimizes the transverse energy gain and produces a beam with low angular dispersion ($< 1°$). With optimum repeller voltages of less than 2 V, beam energy dispersion is typically only ~ 1 eV/charge. Examples of ion trajectories calculated using experimentally determined optimum plate voltages are given in Fig. 3. The sensitivity of the ion gun for N_2^+, defined as the extracted ion current in A per Torr of source pressure and per electron emission current in A, was measured as 13 $Torr^{-1}$ with the source differentially pumped, and 9 $Torr^{-1}$ without pumping. The latter value is close to the theoretical limit imposed by Liouvilles's theorem and compares favorably with other high-yield sources.[18] Although the currents used for calibration are generally small, a high yield is nevertheless required to make up for the low production rates of some ion species (see Table III). The electron beam is generated by either of the two identical electron guns (Figs. 2 and 4). These are designed to provide a well-focused electron beam over a wide range of energies and currents. Electrons are emitted by a 0.1×0.8-cm current-heated tungsten ribbon cathode and are accelerated towards the shield. The cathode is mounted within a slot in the cylindrical repeller electrode. Repeller, lens, and shield electrodes are shaped to produce a concave electric field throughout the acceleration region in order to focus the beam and to offset space-charge forces (similar to a Pierce-type gun[19]). The focal length and lateral position of the beam are controlled by lens and repeller potentials. In order to obtain multiply charged ions as well as to optimize ion yield, the electron energy is variable from < 50 to 1000 eV over the emission current range of 1 μA–3 mA. The performance of the electron gun was checked experimentally by measuring its transmission, which is defined as the ratio of electron current entering the ionization chamber to the total emission current. To simulate real operating conditions the plate potentials were first set for maximum transmission at an emission current of 1 mA and subsequently held fixed. The electron transmission, given in Fig. 5 as a function of emission current, is high ($\sim 70\%$) over most of the operating range, indicating good beam confinement. To illustrate the focal properties, we have included in Fig. 4 some electron trajectories for the space-charge-free case (low currents). At higher currents the focus moves progressively downstream, as the space-charge force increases, until the beamwidth exceeds the diameter of the entry slit at ~ 1 mA. As a consequence transmission decreases rapidly (Fig. 5) at higher currents. The effective electron current, however, continues to increase up to ~ 3 mA. These properties are only weakly dependent on the final electron energy (Fig. 5).

Except for the ion exit slit, the entire ion source region is tightly sealed from the rest of the vacuum system and pumped differentially to minimize backstreaming of sample gas into the main chamber. A gas inlet system with capacity for simultaneously connecting up to seven gas cylinders containing 1 l at 3 atm provides standard pipette volumes of 1.5 cm^3. These are expanded into an intermediate storage volume of ~ 0.2 l, where pure gases or mixtures can be prepared at reduced pressures. In order to increase overall ion production, the sample gas is leaked at a controlled rate directly into the ionization chamber of the ion source by an all-metal needle valve.

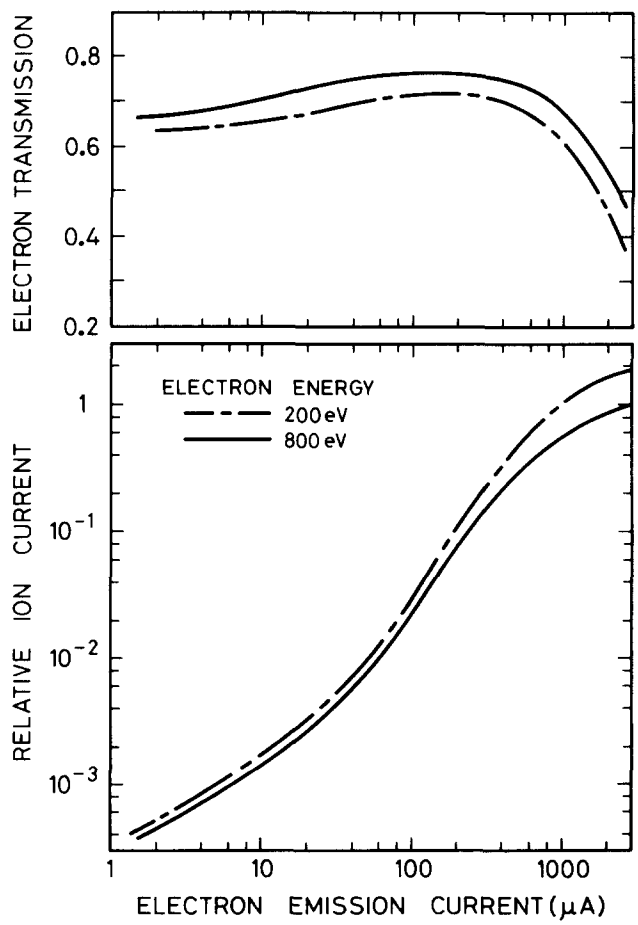

FIG. 5. Transmission efficiency of the electron gun and relative ion (N_2^+) current at the exit of the mass spectrometer as a function of electron emission current. Plate potentials are optimized for maximum ion current at beam energies of 3 keV/charge and 1 mA electron current. Maximum attainable ion current is $\sim 8 \times 10^{-9}$ A.

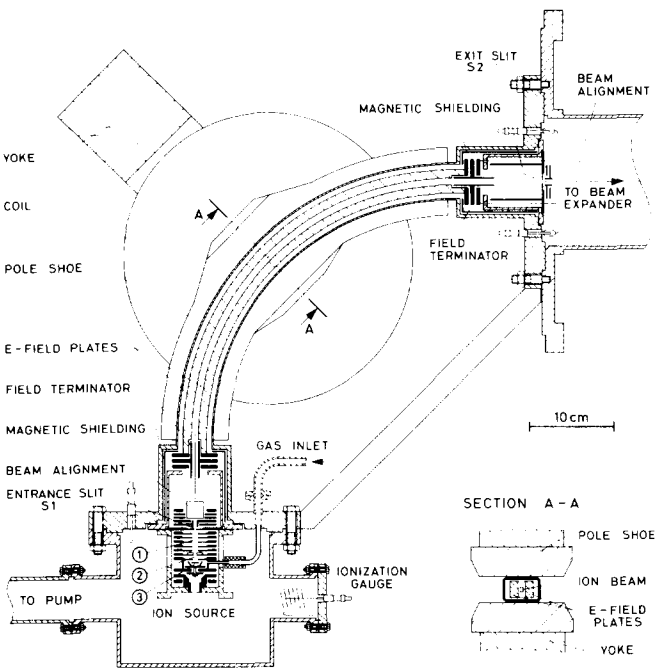

FIG. 6. Plan view of the mass spectrometer with ion source. Central radius is 30 cm, sector angle is 90°, object and image distance are $L1 = L2 = 10.5$ cm, and entrance and exit slit widths are $S1 = 0.06$ cm and $S2 = 0.12$ cm. Key numbers 1–3 are identified in Fig. 3.

Gases which have been used so far, the ion species obtained from these, and the production efficiencies are listed in Table III. The measurements were made with the detector at the exit slit of the system mass spectrometer (Sec. I F) and at an electron emission current of 500 μA, a source pressure of 1×10^{-6} Torr, and a beam energy of 3 keV/charge. All other source parameters were optimized for maximum beam current. These efficiencies, therefore, include mass spectrometer transmission and are thus considerably lower than the efficiency of the ion source alone. The source is capable of delivering most of the ion species described in Tables I and II, including ions with up to nine charge states. The mass/charge range covers species such as Ba^+, used in artificial tracer experiments.[20,21] The maximum beam current that can be achieved with N_2^+ ions is $\sim8\times10^{-9}$ A. Beam currents may be estimated by multiplying the efficiencies by the electron emission current and the pressure and by correcting for nonlinearities in the current characteristics shown in Fig. 5. The ion current is proportional to the pressure measured in the source region up to $\sim5\times10^{-6}$ Torr (N_2), where saturation occurs.

C. Mass spectrometer

The ion beam emerging from the source generally contains several ion species depending on the sample gas and the residual gas. However, calibration of mass spectrometer experiments requires a pure ion beam in order to be able to distinguish between spurious ions originating within the experiment and beam impurities. In order to exclude all undesired ion species from a beam, the ion source is followed by a mass spectrometer. Our design employs a combination of crossed electric and homogeneous magnetic fields in a cylindrical configuration (Fig. 6). The theory of this general class of mass spectrometers is discussed in detail elsewhere.[22,23] The angular focusing condition for a sector-shaped field combination is given by

$$\cot(1+y^2)^{1/2}\phi = \frac{(1+y^2)^{1/2}}{R}\,\frac{L1L2 - R^2(1+y^2)^{-1}}{L1+L2}, \tag{1}$$

where ϕ is the sector angle $L1$ and $L2$ are the object and image distances from the sector boundary and R is the central radius of curvature. The dimensionless parameter y is the ratio of electric to centrifugal force

$$y = 1 - cRB\left(\frac{M}{Z}\frac{E}{Z}\right)^{-1/2}, \tag{2}$$

where B is the magnetic induction, M/Z the mass per charge and E/Z the energy per charge of the ion, and c is a constant. Condition (1) is satisfied by two values of $y(=\pm y_0)$ for any given geometry since y enters quadratically. Thus there are always two combinations of electric and magnetic fields that give rise to angular focusing. The special case where $y^2 = 1$ is of particular interest since it represents the ordinary electrostatic analyzer ($y = +1, B = 0$) and a mass spectrometer ($y = -1, B \neq 0$). The analyzer is designed to take advantage of this and is thus capable of producing either mass/charge analyzed or mixed mass beams. We have employed similar ion optical designs in mass spectrometers flown on a number of spacecraft.[11,12,14] A double focusing mass spectrometer of this type has been applied in the laboratory.[24]

The general construction of the mass analyzer is evident from Fig. 6. The magnetic field is generated by an electro-

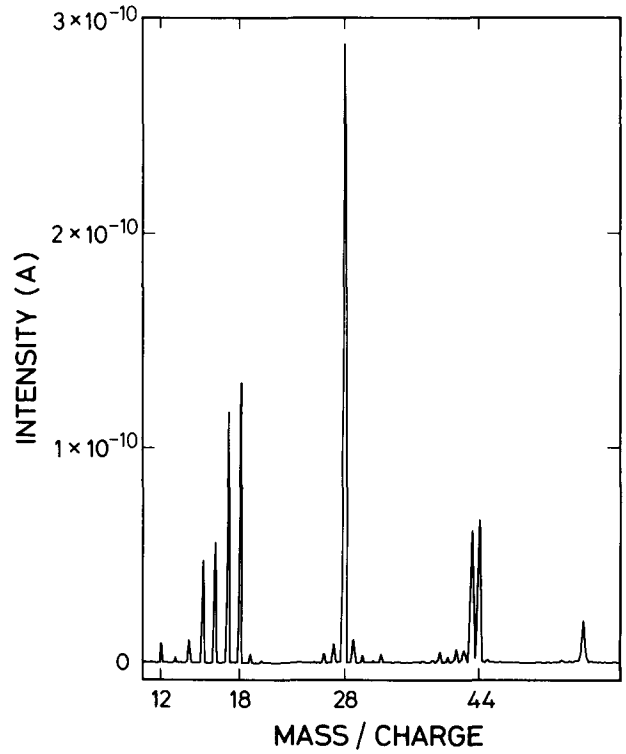

FIG. 7. Mass spectrum of residual gas and leaked N_2 gas obtained by scanning the magnetic field with the electric field turned off (low-resolution mode). Ion energy is 3 keV/charge. Mass/charge = 18 (H_2O^+) is obtained at a sensitivity of 30% of the other peaks.

magnet designed to be sufficiently stable to maintain the mass-selected beam over a period of several days. Magnetic fields up to 0.3 T are produced across a gap of 3.0 cm. The electric field is generated by a pair of cylindrical deflection plates (0.8-cm separation) that are suspended between pole pieces inside the vacuum tube. The potential applied to these plates is derived from the ion source voltage via a voltage divider. A 90° sector angle was chosen to minimize overall dimensions. To minimize magnetic and electric stray fields in the drift regions, magnetic shielding and electric field terminators have been added. Proper ion beam alignment is obtained by means of pairs of horizontal and vertical deflection plates located at the entrance and exit of the spectrometer.

The highest mass resolution in this design is achieved when the magnetic force is centripetal and the electric force is equal to the centrifugal force in direction and magnitude (case $y = -1$). Since the magnetic induction is limited, only the lower portion of the mass range from 1 to 50 amu can be covered in this mode by scanning the magnetic field. Higher masses from 50 to 150 amu are obtained by reducing the electric field while keeping the magnetic field constant. Since the focal point moves away from the exit slit S2 during this process, resolution decreases gradually. Because of the effects of electric fringing fields, the mass resolving power of the present system is below the design goal of 150 needed to completely separate $^4He^{++}$ from H_2^+. An improved version employing fringing field correction electrodes is presently being designed.

The spectrometer may be conveniently operated as an ordinary sector magnet by turning the electric field off ($y = 0$ case). Although the focusing condition (1) is no longer satisfied, mass resolution is sufficient for most applications. A sample mass spectrum obtained in this low-resolution mode by scanning the magnetic field is shown in Fig. 7. Mass resolution $M/\Delta M$ is approximately 50 at $M/Z = 40$ and 10% of peak height. The production efficiencies for the various ion species given in Table III were determined using this mode. When used as an electrostatic analyzer to produce a mixed-ion beam while maintaining angular focusing, the magnetic field is switched off and the electromagnet moved away from the sector to avoid interference from remnant magnetic fields.

D. Beam expander

Since the size of the ion beam at the exit of the mass spectrometer is very small (0.1×0.8 cm), the area of the ion beam must be enlarged considerably to cover the typical entrance aperture of the plasma instrument to be calibrated. The expansion system shown in cross section in Fig. 8 increases the beam area by a factor of up to 5×10^3 and provides a uniform intensity distribution. In order to avoid a strong correlation between beam size, intensity, and energy, expansion is carried out before the final acceleration stage. Expansion is accomplished by first rastering the pencil beam over a certain area and then decelerating the ions to low energy. After allowing them to drift transversely they are accelerated back to their original energy.

The modulator section (Fig. 8) consists of pairs of horizontal and vertical deflection plates. By adjusting dc voltages across the plates the beam is centered along the drift tube. Superimposing triangular waveform voltages rasters the pencil beam across a selected area. The amplitudes of the sweep voltages are adjustable from 0 to 200 V, adequate to sweep out an area of 10×20 cm at grid G1. Since the beam must evenly illuminate the target area, a triangular waveform is used. To obtain symmetric deflection, the sweep voltages applied to a plate pair are out of phase by 180°. Frequencies are adjustable from 1 to 50 kHz for horizontal deflection and 0.1 to 5 kHz for vertical. These are chosen to be much faster than any instrument measurement cycle to prevent sampling biases. A uniform intensity distribution also requires that the scan traces overlap significantly. Given the relatively large spot size at the target (Fig. 10), a frequency ratio of ~ 10 is found sufficient to produce the desired effect.

The drift section is made up of four high-transparency-

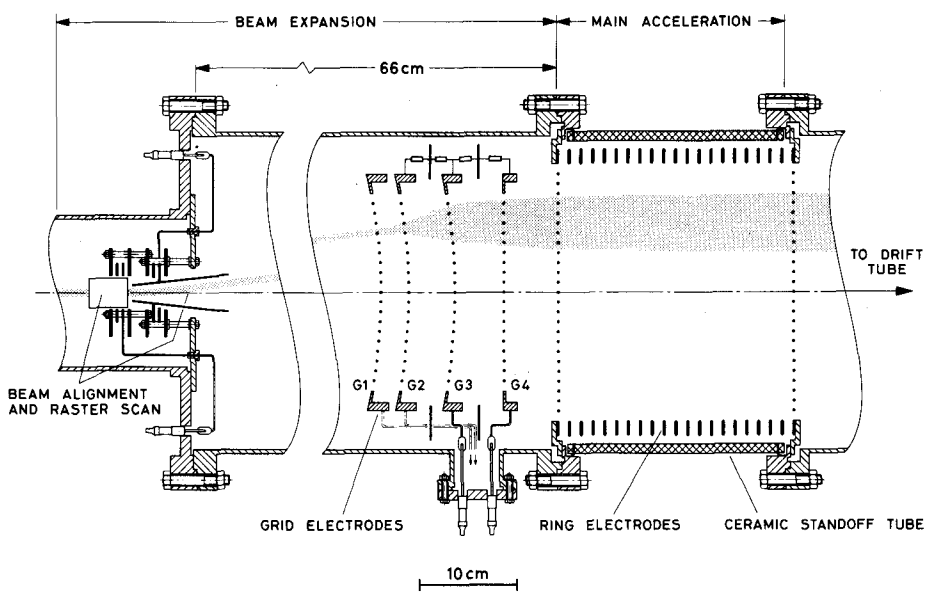

FIG. 8. Vertical cross section of beam expander and main accelerator. The beam is rastered by triangular ac voltages (up to 50 kHz, up to 400 V peak to peak) applied to deflection plates and decelerated from 3000 to ~ 10 eV/Z between G1 and G2. Ring electrodes are connected to an internally mounted resistor chain.

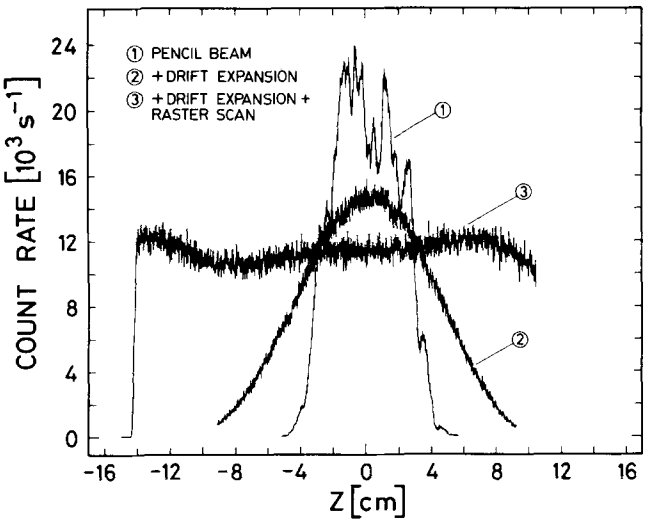

FIG. 9. Vertical beam profiles for a 10-keV/Z ion beam, measured with the CEM beam profile detector. Unexpanded pencil beam (1), drift expanded (2), and raster plus drift expanded beam (3).

grids (total transmission $\sim 65\%$) measuring 12×22 cm. The ions are first decelerated between the concentric cylindrical grids G1 and G2. The combined effect of deceleration and scattering in the microfield of the grid wires strongly increases the angular divergence of the ion beam. After drifting to grid G3 at energies adjustable between 0 and 150 eV, ions are accelerated back to 75%–100% of the original energy at G4. The net effect of the drift section is to increase the size of the pencil beam and to smooth out small-scale irregularities caused by grid wires (Fig. 9), thus enabling use of a coarser raster pattern. This also reduces the intensity modulation of beam current which may otherwise introduce saturation problems in detectors with limited dynamic range. By combining both of the expansion methods discussed above, it is possible to achieve homogeneity of $\pm 5\%$ over large areas up to ~ 250 cm^2 (Fig. 10).

E. Main acceleration and drift tube

After beam expansion, ions are postaccelerated or decelerated in one or both of the drift tube sections indicated in Fig. 1. The final energy is given by the sum of the fixed ion source voltage (3 kV usually) and the main acceleration voltage (-3 to $+99$ kV). The main acceleration voltage must be applied to the entire source section preceding the drift tube (Fig. 1). Hence this section is entirely enclosed in a sheet metal cage that is placed on high-voltage stand-off insulators. A grounded Faraday cage completely surrounds the assembly, with a separate cage housing the control electronics and two 1000-W transformers that deliver the required power.

Voltages are measured by means of high-precision (0.1%) Ohmic dividers. An alumina ceramic tube containing the main acceleration element provides an electrically insulating vacuum connection between the drift tube and the source section. This tube has a diameter of 30 cm and a length of 21 cm and is capable of withstanding 100 kV. The main acceleration electric field is formed by 21 equally spaced parallel ring electrodes (Fig. 8) which derive their potential from a high-impedance precision resistor chain. These resistors are integrated into the electrode design and divide the applied voltage evenly. To contain and terminate the field, the first and last ring electrodes are constructed with a high-transmission (98.5%) curtain of parallel wires 0.0034 cm in diameter spaced 0.4 cm apart. Besides producing a highly homogeneous electric field (to within $\sim 1\%$) over a large diameter (26 cm), this design also minimizes the formation of beam contaminants through secondary ion emission from grid wires. Although ions experience some transverse acceleration in the microfield near the grid wires, the effect on beam spread is small as inferred from pencil beam profiles (Fig. 9). All insulating surfaces are effectively shielded from the beam throughout the acceleration and drift regions.

In order to further improve beam size, homogeneity, and parallelism, a 350-cm-long passive drift section is included between the main acceleration region and the instrument platform. A 300-cm-long drift tube with an inner diameter of 32 cm connects the source section with the main chamber. The drift tube contains two pairs of large deflection plates for correcting misalignment of the beam and is electrically insulated from ground and from the main chamber by a 10-cm-long ceramic tube. An additional deceleration element consisting of a pair of parallel grids spaced 1.0 cm apart with an inner aperture of 26 cm can be inserted

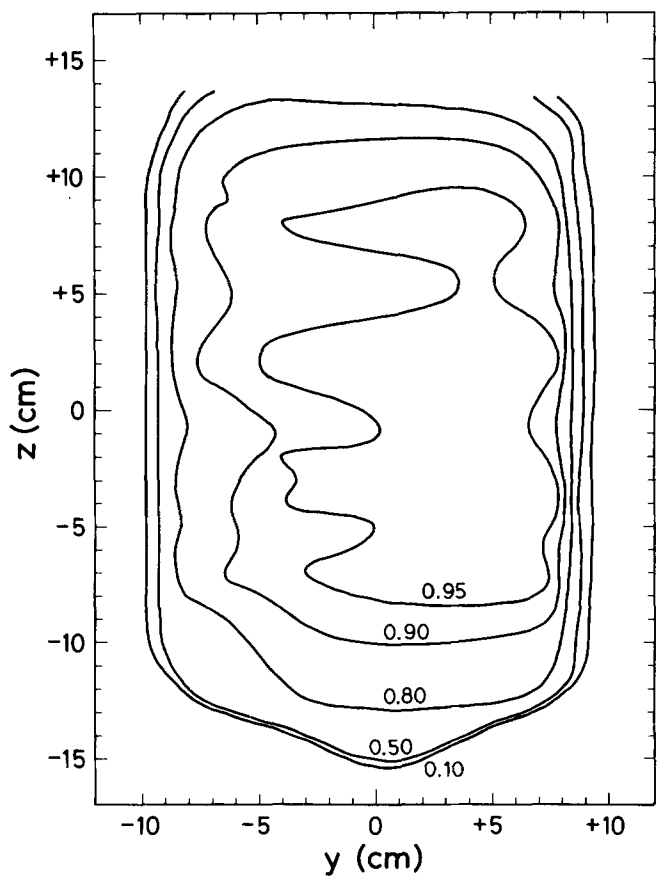

FIG. 10. Isointensity contours of expanded 30-keV/Z ion beam obtained with the CEM beam profile detector.

into this insulation tube via the main chamber when needed, but is otherwise removed to avoid shadowing and scattering effects.

To obtain energies less than the ion source voltage of 3 kV, a deceleration voltage (negative) is applied. Since deceleration increases the angular spread, beam intensity decreases, particularly at energies <0.1 keV/Z (Fig. 11). Higher beam intensities may be obtained by deferring the deceleration either partially or completely to the end of the drift tube. This requires floating the entire drift tube to a negative potential between 0 and -3 kV, although the significant loss of beam parallelism due to this operation may not be acceptable in a particular application.

F. Beam diagnostics

Several diagnostic detectors placed at key points along the beam path provide the capability for optimizing various subsystems and for continuously surveying the beam. Besides being used during initial beam setup, these detectors also furnish beam parameters required during calibration. The detectors are described below in order of distance away from the ion source.

The mass spectrometer detector is mounted on a linear motion feedthrough and intercepts ions passing through the exit slit of the mass spectrometer (Fig. 6). It is used to fine-tune the ion and electron guns and the mass spectrometer, and to select the desired ion species. The detector contains a Faraday cup for measuring ion currents in the range from 10^{-8} to 10^{-12} A as well as an electron multiplier (RCA C 70129 D), operated in the current mode, for lower currents.

The beam scanner measures the two-dimensional intensity distribution and absolute beam current just ahead of the target instrument at the drift tube entry port into the main chamber. It contains a channel electron multiplier (CEM) and a Faraday cup mounted on vertical and horizontal slide bars. The entire scanner is motor driven independently in two directions over the entire 30-cm beam diameter. Positioning is controlled to within ≈ 0.05 cm by means of precision linear resistors.

The Faraday cup is used as an absolute current standard to determine detector efficiencies and cross-calibrate beam diagnostic CEM's. Consequently it has a large area of 5 cm^2 in order to have sufficient overlap with the counting detectors and to be capable of measuring currents as low as 10^{-15} A/cm^2. The cup collector is covered with a tightly wound spiral of 0.02-cm copper sheet that acts as a baffle to reduce losses through backscattered particles. Two suppressor electrodes elminate secondary electrons and spurious ions from gauges and pumps. Other design features include good mechanical rigidity and electrical shielding of the collector, low contact potentials through gold plating of all surfaces, and high impedance of all electrical standoffs.

The cup signal is amplified by a low bias current operational amplifier (Teledyne Philbrick 1702) using a 10^{12}-Ω feedback resistor. All elements of the amplification circuit are placed in a vacuum-tight container filled with dry helium. To minimize the length of the signal lead, the container is mounted directly to the guard shield and the input is connected to the Faraday cup via a high-impedance vacuum feedthrough. With this design, currents as low as 4×10^{-15} A have been measured with time constants ~ 25 s.

A fraction of the ion beam is allowed to pass through a central aperture ($\phi = 0.6$ cm) in the Faraday collector to a CEM located behind the assembly. This CEM, with a sensitive area of only 0.1 cm, is used primarily to obtain beam intensity profiles and to track temporal changes during the integration time of Faraday cup current measurements. It is operated with the collector at ground potential and with a negatively biased repeller electrode in front of the funnel. Pulses are amplified by a preamplifier–pulse shaper situated in the detector module. The output signal is converted to an analog voltage and plotted versus horizontal or vertical position on an X–Y recorder. Examples of beam profiles are shown in Figs. 9 and 10. By combining measurements of (a) the absolute beam current, (b) the relative intensity distribution over the entrance aperture of the Faraday cup, and (c) temporal changes in both of these, the efficiency of the CEM detector can be calculated.

The beam monitor is a CEM detector with a maximum sensitive area of 1.0 cm^2 placed near the instrument entrance aperture to continuously survey the beam current. Some matching of beam monitor dynamic range to that of the instrument under calibration can be achieved by reducing this area. The time-consuming process of establishing the response of an instrument requires constant beam intensity. This is obtained with a feedback circuit which transmits the beam monitor countrate via a fiber optics cable to the emission control unit. After conversion to an analog voltage the signal is compared to a preset reference and is differentially amplified and used to control the emission current of the electron gun. This method operates over the range of electron emission current shown in Fig. 5 and at ion currents as low as 10^{-16} A. Basically the speed of the feedback circuit is limited by the thermal inertia of the cathode. The raster frequencies of the beam expander (>1 kHz) are chosen to be much faster than the cathode response, whereas the latter is

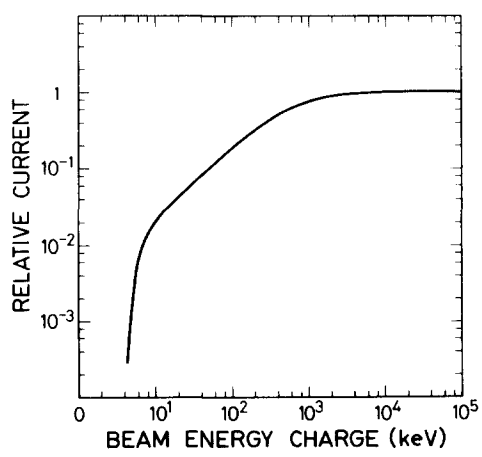

FIG. 11. Ion current as a function of beam energy/charge at the instrument platform. Beam area and uniformity are adjusted to ~ 100 cm^2. The ratio of ion current (A/cm^2) at the instrument platform to that at the mass spectrometer exit is $\sim 8\times 10^{-4}$ at 3 keV/Z.

faster than the energy scan period (~ 1 s). Consequently, no beam intensity modulations appear at frequencies sensible to the instrument under calibration.

G. Experiment chamber

The experiment section of the calibration system is a cylindrical chamber 120 cm in diameter and 300 cm long. It is split at about 1/3 of its length, with the shorter section mounted on rails for easy access to the experiment mounting area. The chamber is equipped with a gimballed turntable that accommodates experiments weighing up to ~ 12 kg with dimensions up to $\sim 30 \times 40 \times 75$ cm. These can be mounted such that the center of the entrance aperture is aligned with the two centers of rotation of the turntable and with the beam axis. The turntable can be rotated with a precision of 0.1° through $-90°$ to $+90°$ in azimuth (α) and $-35°$ to $+75°$ in elevation (β). The externally controlled motions are derived from linear motors mounted in vacuum-sealed containers within the chamber.

H. UHV system

High beam purity is necessary for the testing and calibration of sensitive mass spectrometers. This requires a clean UHV environment operating at pressures $\lesssim 10^{-8}$ Torr. Under ion bombardment, residual hydrocarbon gases can lead to the formation of insulating surface layers that may become charged. Furthermore, heavy hydrocarbons have been implicated in the degradation of detectors such as CEM's.[25] Thus particular attention was given to the cleanliness of construction materials and pumps. All chamber sections are built of stainless steel. In order to obtain a good surface conductivity and low ion sputtering yields,[26] all surfaces that are in contact with the ion beam are gold plated. Joints and ports are sealed by means of gold or copper gaskets with the exception of the main chamber access port and the drift tube shutter valve which use Viton A. Glass, sapphire, and alumina are used for insulating mounts. Organic materials with low outgassing at the relevant temperatures ($\lesssim 200$ °C) were used in limited quantities in the main chamber section: polyimid gliding mounts, Kel-*F* insulators, and PTFE cables.

The main chamber can be sealed off from the drift tube by means of an automatic 30-cm-diam shutter valve, and both can be pumped separately. This allows the main chamber to be accessed while preserving good vacuum in the source section. The ion source itself is pumped differentially by means of a turbomolecular pump to limit back streaming of leaked sample gases into the chamber. All sections and components of the system are individually bakable to 250 °C. Vacuum is obtained with turbomolecular, diode ion-getter, and titanium sublimation pumping combined with a liquid freon cold panel. The final pressure attained after approximately 2–3 days is $\sim 10^{-9}$ Torr under clean conditions.

Since spaceflight instruments present heavy outgassing loads (due to thermal paints, conformal coatings, and electronics components), they are preconditioned with a mild bakeout in a second vacuum system. If possible, the electronics are also operated at this time to thoroughly outgas all parts.

II. PERFORMANCE

Beam energy. The facility is capable of producing ion beams with continuously adjustable energy up to a design goal of 100 keV/charge (the maximum beam energy achieved so far is 90 keV/Z). However, at energies $\lesssim 5$ eV/Z the intensity decreases below useful levels as a result of beam dispersion along the drift path (Fig. 11). Depending on the final energy E, the energy spread of the ions is dominated either by the source (10^{-3} keV/Z) or by the HV power supply ripple (R) according to Eq. (3):

$$\Delta E/E = [1 \times 10^{-3} + R\,|(E-3)|\,]E^{-1}. \quad (3)$$

Thus, at very low energies the relative energy inhomogeneity becomes quite large, reaching $\sim 10\%$ at 10 eV/Z, since the 20-kV power supply ripple is $\sim 1 \times 10^{-4}$. It decreases steadily with increasing energy to $\sim 10^{-3}$ at $E > 20$ keV/Z (typically $R \sim 1 \times 10^{-3}$), a value that is small compared to the energy passbands ($\gtrsim 1\%$) of typical space plasma analyzers. Thus, the ion beam is nearly monoenergetic for $E \gtrsim 100$ eV/Z.

During calibration, the beam energy must be varied in order to cover the entire passband of the analyzer uniformly. This can be accomplished by discrete stepping of the main acceleration voltage using externally programmable power supplies. Alternatively, the beam energy may be scanned continuously by means of the energy modulator, a 0–3-kV operational power supply inserted in series with the main acceleration voltage (Fig. 11). This circuit is designed to perform two functions. In one mode the output voltage is ramped linearly through the energy passband once per experiment accumulation cycle with a scan period of ~ 1 s. The start of the ramp can be triggered externally to coincide with the accumulation cycle. A second mode simulates a beam with a wide energy spread by producing a triangularly modulated output voltage with an adjustable frequency between 10 and 50 Hz. This frequency is much lower than the raster frequency of the beam expander (> 1 kHz). Hence, position and energy are randomly mixed. However, to avoid biasing the measurements, the experiment sampling period should not be much shorter than ~ 1 s in this mode.

Angular divergence. The divergence of the ion beam was measured using a pinhole detector "camera" with an intrinsic angular resolution at full width of 0.1°. The detector was mounted on the turntable with its axis aligned with the drift tube. All three examples of angular distributions shown in Fig. 12 were obtained under similar conditions of beam homogeneity over an area of ~ 100 cm^2. The beam is seen to be highly parallel, its angular spread being $\sim 0.3°$ at FWHM and $\sim 1°$ at 10^{-4} of peak intensity. If deceleration is deferred to the end of the drift tube, the angular spread increases substantially at energies < 1 keV/Z.

Beam intensity. The maximum current delivered at the instrument platform after optimizing all source-parameters is mainly limited by ion production efficiency (Table III). In addition, beam expansion and losses incurred in the mass spectrometer and drift region significantly decrease the current density. This is seen in Fig. 11 which gives the fraction of the total current leaving the mass spectrometer that arrives at the experiment platform (per cm^2). These results

were obtained by varying the main acceleration voltage while keeping the cross-sectional area of the beam fixed at ~ 100 cm^2. We note that a substantial decrease in intensity occurs at energies below ~ 10 eV, mainly as a result of an uncontrollable increase in beam spread beyond 100 cm^2. Somewhat higher intensities can be achieved by decelerating the beam at the end of the drift tube. Using Fig. 11, the current density at the experiment platform may be estimated from production efficiencies (Table III) and the ion source characteristics (Fig. 5). Typical maximum fluxes for a H_2^+ beam are $\sim 10^7$ cm^{-2} with a wide beam (~ 100 cm^2) and $\sim 10^8$ cm^{-2} with a pencil beam (expander turned off).

To illustrate the current monitoring capabilities of the beam scanner, included in Fig. 13 are results of a cross calibration between the beam profile and the absolute current detectors. The two detectors together cover the necessary range of beam currents, extending from $\sim 10^{-18}$ to $\sim 10^{-12}$ A/cm^2 with significant overlap. Absolute current measurements are limited by the bias current of the operational amplifier to $\sim 2\times 10^{-15}$ A.

Beam uniformity. A two-dimensional intensity contour plot of a 30-keV H_2^+ beam measured with the beam profile detector is shown in Fig. 10. In this example the beam expander was set to maximize beam area. Uniformity is $\pm 5\%$ over an area of ~ 250 cm^2 and $\pm 25\%$ over ~ 500 cm^2. The FWHM of the beam is 18 cm in the horizontal and 28 cm in the vertical direction. The spot size of the pencil beam is $\sim 2\times 2$ cm at high energies, increasing at lower energies.

Beam stability. A sufficiently stable beam intensity for short-term applications is obtained by regulating the cathode heater current and the gas leak rate. However, to maintain the intensity at a selected level for extended periods (hours to days), the ion current feedback circuit described in Sec. I F must be used. With this circuit the long-term drift in the intensity is less than 1% over 10 h. The stability with respect to changes in the ion source pressure is $\sim 5\%$ for a pressure change from 2×10^{-7} to 2×10^{-6} Torr.

Beam purity. Particles with energy/charge, mass/charge, and angles differing from those of the primary ions are considered beam contaminants. These are continuously injected into the beam by collision processes, but also result from the finite mass dispersion of the mass/charge analyzer. Since it is difficult and often impossible to uniquely distinguish a contaminant from a spurious signal arising within the instrument being calibrated, beam purity should be better than the planned rejection rate of the instrument. The following discussion serves to briefly outline some of the more important effects.

One of the factors affecting beam purity is the vacuum environment. Residual gases are ionized in the ion source and remain in the beam if their mass per charge ratio is nearly equal to that of the desired ion species. The resulting interference is particularly noticeable when the desired ion has a low production efficiency, such as $^{16}O^+$ or $^4He^{2+}$. For example, assuming the residual gas is CH_4 and H_2 at a partial pressure of 1×10^{-9} Torr and using CO_2 or He as a leak gas at 1×10^{-6} Torr, the estimated interferences are $\sim 1\%$ for $[CH_4^+/O^+]$ and $\sim 10\%$ for $[H_2^+/He^{2+}]$, respectively. In the case of H_2^+ and He^{2+} the actual interference is smaller because the mass spectrometer partially separates the two ions.

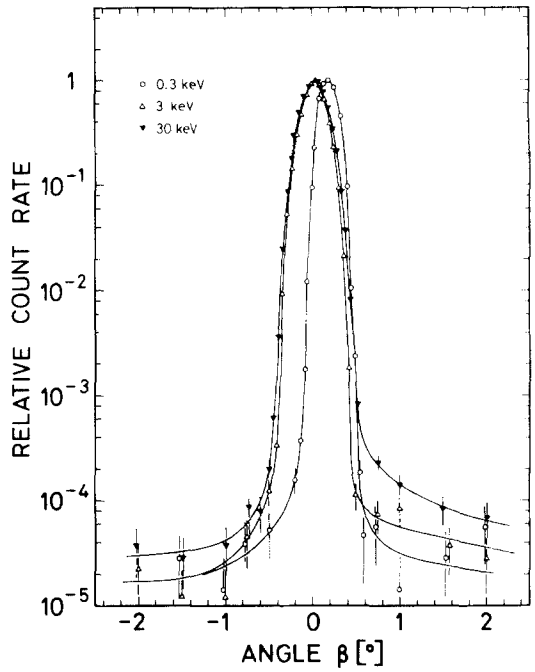

FIG. 12. Angular distribution of the expanded ion beam (~ 100-cm^2 area) at the instrument platform for three different ion energies.

Ion scattering within the mass spectrometer gives rise to a spurious background which again is more significant for minor ion species. This interference is usually less than 10^{-4}. Furthermore, collision processes with residual gases such as scattering, ionization, charge transfer, and dissociation produce a complex mixture of particles with energies ranging from a few electron volts up to and beyond the energy of the primary. Of these, charge transfer is most effective because of its high cross section. If the chamber is filled with a leak gas (e.g., He or N_2) at $\sim 10^{-6}$ Torr, this process may intro-

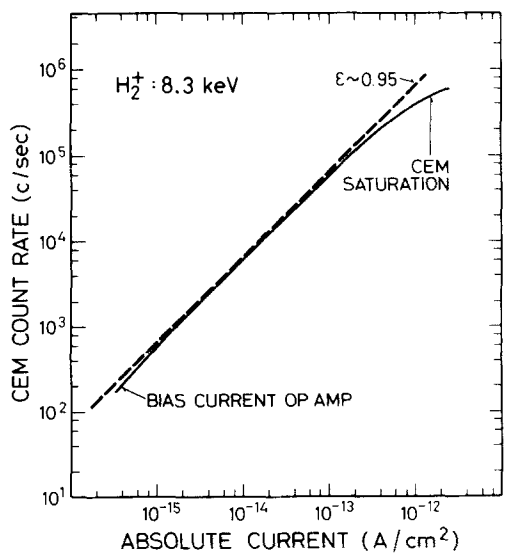

FIG. 13. Cross calibration of the beam scanner detectors with 8.4-keV H_2^+ ions. The sensitive area of the CEM is 0.1 cm^2, of the Faraday cup 5 cm^2.

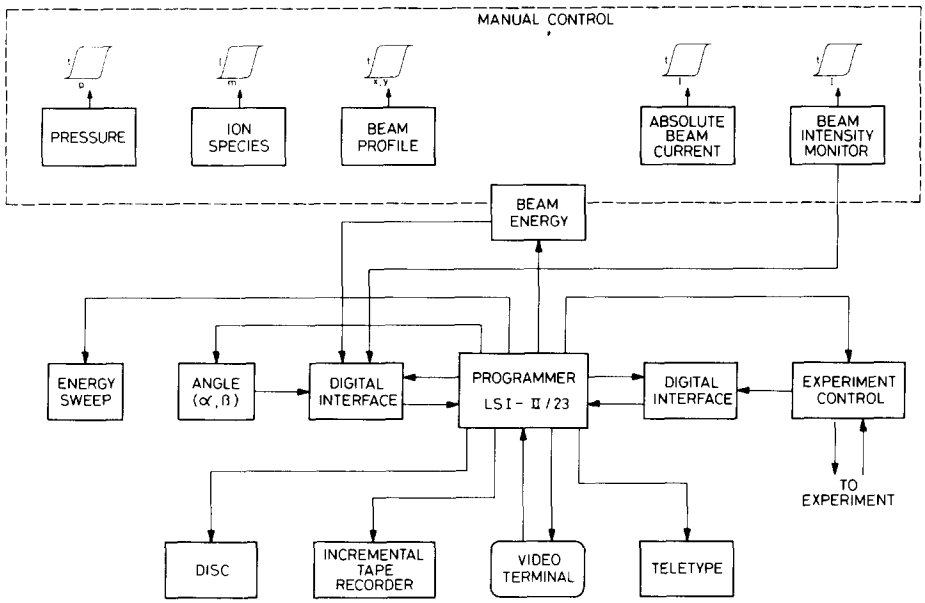

FIG. 14. Block diagram of calibration control and monitoring.

duce impurities exceeding 1%. Thus, in order to reduce beam contamination to $\sim 10^{-5}$, the system pressure should be $\lesssim 10^{-8}$ Torr. In collisions with walls and electrodes of the system, surface adsorbed gas and metallic ions are sputtered with relatively high yields of $\sim 10^{-3}$.[26] The most critical part of the system is the main acceleration region where these ions may be extracted with high efficiency at energies close to the primary (less $\lesssim 3$ keV/Z). These have not been observed experimentally at an intensity $\gtrsim 10^{-5}$ of the primary. Furthermore, since all surfaces are gold plated, sputtered gold ions are easily identified by their large mass.

III. CALIBRATION

The experiment to be calibrated is mounted, usually together with its electronics package, on the turntable. The ion beam is then set to uniformly irradiate the entire entrance aperture of the experiment and the instrument response is recorded while internal voltages (i.e., on deflection plates or grids) are ramped through their active range. Calibration parameters are usually changed in order of increasing complexity: α angle (fastest), β angle, beam energy, and ion species (slowest). Orientation angles α and β with respect to the beam are preprogrammed to cover the full solid angle of acceptance of the experiment. A single angular step is done fairly rapidly in ~ 5 s. Large changes in ion beam energy, particularly below 5 keV/Z, necessitate some adjustments to beam parameters and remeasurement of the beam profile, which may require $\sim 1/2$ h. Changing the ion species requires the largest number of adjustments to the beam system and, hence, a particular ion species may be run for one or more days. Except for the angular scan and the energy sweep, all other calibration parameters require operator intervention. The actual data taking is partially automated through the use of a minicomputer (Fig. 14). The data are stored on tape or disk for later analysis but can also be processed in real time for quick display on a video terminal.

Basically there are three objectives in calibrating a satellite-borne mass spectrometer: (1) absolute calibration to determine experiment sensitivity at normal beam incidence, (2) energy-angle response measurement which allows the energy-geometric factor to be calculated, and (3) determination of mass peak shape and a search for spurious mass signals. Absolute calibration (1) is made by comparing the known incident bean intensity (ions/cm^2 s) with the measured counting rate per second. This ratio includes the product of detector efficiency, instrument transmission, and sensitive area. The energy-geometric factor (2), usually normalized to the count rate in (1), is obtained by taking appropriate averages over the angular and energy response. Peak shapes (3) are determined with the same set of scans as (2). The search for ghost peaks (3) is carried out using a mono-mass beam and scanning the detector over a selected mass-energy region surrounding the location of the beam in mass-energy space.

All three types of measurements must take into account

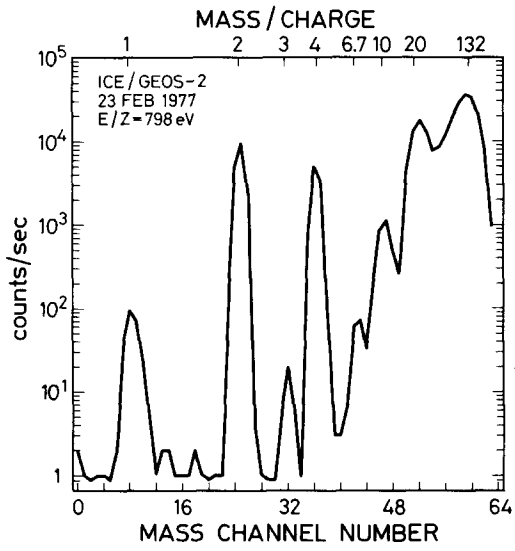

FIG. 15. Calibration result of GEOS Ion Composition Experiment. Experiment was subjected to an 800-eV/Z ion beam with a wide energy spread. Gases leaked in the ion source were H_2, He, Ne, and Xe. Mass spectrum was obtained by integration over all angles.

that the experiment response varies with ion species, energy, and angle. Thus it is generally of advantage to record the individual distributions rather than an integral. By properly weighting and combining these, it is then possible at a later time to simulate the experiment response to any distribution of incident flux. In the calibration of the GEOS spectrometers we recorded nearly complete mass spectra at each α, β point. Summation of these over all angles then yielded mass peaks having $\sim 10^6$ counts, so that peak shape was well defined and ghost peaks were evident at the 10^{-5} level (Fig. 15).

Obviously it is not possible to carry out a thorough program covering the entire mass-energy-angle space. Considering that five ion species are involved and that typical detectors may have 30 energy levels, ~ 30 mass steps, and fields of view requiring ~ 300 angular steps, then $\sim 10^6$ separate measurements are required. Assuming each data sample is ~ 1 s and including set-up times, then ~ 200 working days are needed to collect data. In practice, calibration must be confined to strategically selected subregions of the parameter space. This yields a satisfactory calibration, provided some theory of the instrument optics is available to guide in interpolation of the data. It is useful for this purpose to first map out the parameter space by making a rough cut at the instrument response. Using this method, for example, GEOS ion composition experiment calibration required ~ 2 months.

ACKNOWLEDGMENTS

We are indebted to a large number of people that have been involved with the development of the facility over a period of eight years. We thank in particular J. Fischer, H. Hofstetter, H. Wyniger, W. Siegenthaler, and H. Lüthi for engineering and mechanical development, and R. Liniger, M. Neuenschwander, and J. Stettler for electrical design and construction. Valuable assistance has been given by H. P. Walker, L. Weber, and P. Wägli. We acknowledge the technical assistance of M. Colomb and P. Rosenberger. We are grateful to H. Rosenbauer for valuable advice and technical contributions, and to E. G. Shelley for useful discussions. We wish to thank L. Reichert and B. Papritz for typing the manuscript.

This work was supported by the Swiss National Science Foundation under consecutive grants 2.405.70 through 2.255.81. One of us (D.T.Y) acknowledges support by the U. S. Department of Energy during preparation of the manuscript.

[a] Present address: Space Sciences Laboratory, Lockheed Palo Alto Research Laboratory, Palo Alto, California 94304.
[b] Present address: Los Alamos National Laboratory, Los Alamos, New Mexico 87545.

[1] H. Balsiger, Adv. Space Res. (in press, 1982).
[2] F. R. Paolini and G. C. Theodoridis, Rev. Sci. Instrum. **38**, 579 (1967).
[3] G. C. Theodoridis and F. R. Paolini, Rev. Sci. Instrum. **39**, 326 (1968).
[4] G. C. Theodoridis and F. R. Paolini, Rev. Sci. Instrum. **40**, 621 (1969).
[5] W. Riedler, Ark. Geofys. **5**, 637 (1971).
[6] A. D. Johnstone, Rev. Sci. Instrum. **43**, 1030 (1972).
[7] P. Christophersen, Ark. Geofys. **5**, 659 (1971).
[8] R. L. Arnoldy, P. O. Isaacson, and D. F. Gats, Rev. Sci. Instrum. **44**, 172 (1973).
[9] T. R. Sanderson and J. Henrion, Space Sci. Instrum. **1**, 351 (1975).
[10] J. Geiss, Proc. 13th Int. Cosmic Ray Conf. **5**, 3375 (1973).
[11] H. Balsiger, P. Eberhardt, J. Geiss, A. Ghielmetti, H. P. Walker, and D. T. Young, Space Sci. Instrum. **2**, 499 (1976).
[12] E. G. Shelley, R. D. Sharp, R. G. Johnson, J. Geiss, P. Eberhardt, H. Balsiger, G. Haerendel, and H. Rosenbauer, IEEE Trans. Geosci. Electron. **GE-16**, 266 (1978).
[13] M. A. Coplan, K. W. Ogilvie, P. A. Bochsler, and J. Geiss, IEEE Trans. Geosci. Electron. **GE-16**, 185 (1978).
[14] E. G. Shelley, A. Simpson, T. C. Sanders, E. Hertzberg, H. Balsiger, and A. Ghielmetti, Space Sci. Instrum. **5**, 443 (1981).
[15] H. Balsiger, J. Geiss, D. T. Young, H. Rosenbauer, R. Schwenn, W.-H. Ip, E. Ungstrup, M. Neugebauer, R. Goldstein, B. E. Goldstein, W. T. Huntress, E. G. Shelley, R. D. Sharp, R. G. Johnson, A. J. Lazarus, and H. S. Bridge, ESA SP-169 (1981), p. 93.
[16] M. Neugebauer, D. R. Clay, B. E. Goldstein, and R. Goldstein, Rev. Sci. Instrum. **53**, 99 (1982).
[17] A. O. Nier, Rev. Sci. Instrum. **11**, 212 (1940).
[18] D. L. Swinger, J. Appl. Phys. **41**, 1496 (1970).
[19] J. R. Pierce, J. Appl. Phys. **11**, 548 (1940).
[20] D. T. Young, in *The Scientific Satellite Programme During the International Magnetospheric Study*, edited by Knott and Battrick (Reidel, Dordrecht, Holland, 1976), p. 397.
[21] D. T. Young, Adv. Space Res. **1**, 305 (1981).
[22] W. Henneberg, Ann. Phys. (Leipzig) **19**, 335 (1934).
[23] R. Herzog, Z. Phys. **89**, 447 (1934).
[24] D. Fischer, Z. Phys. **133**, 471 (1952).
[25] B. D. Klettke, N. D. Krym, and W. G. Wolber, IEEE Trans. Nucl. Sci. **NS-17**, 72 (1970).
[26] K. Wittmaack, in *Inelastic Ion-Surface Collisions*, edited by N. H. Tolk, J. C. Tuely, W. Heiland, and C. W. White (Academic, New York, 1979), p. 153.